



White fungus-like mesoporous Bi₂S₃ ball/TiO₂ heterojunction with high photocatalytic efficiency in purifying 2,4-dichlorophenoxyacetic acid/Cr(VI) contaminated water

Lixia Yang^a, Wensi Sun^a, Shenglian Luo^{a,b,c,*}, Yan Luo^a

^a High Level Laboratory of Jiangxi Province for Persistent Pollutants Control, Recycle and Reuse, Nanchang Hangkong University, Nanchang 310063, PR China

^b State Key Laboratory of Chemo/Biosensing and Chemometrics, Hunan University, Changsha 410082, PR China

^c Department of Chemistry and Chemical Engineering, Key Laboratory of Environmental Biology and Pollution Control, Hunan University, Changsha 410082, PR China



ARTICLE INFO

Article history:

Received 13 October 2013

Received in revised form 20 February 2014

Accepted 23 February 2014

Available online 3 March 2014

Keywords:

Mesoporous Bi₂S₃ balls

Heterojunction

Photocatalytic degradation

2,4-dichlorophenoxyacetic acid

Cr(VI)

ABSTRACT

Single crystalline, three dimensional (3D) white fungus-like mesoporous Bi₂S₃ crystals were modified onto the TiO₂ nanotube (NT) arrays by pulsed electrodeposition technique which constructs a unique heterojunction photocatalyst bearing large surface area and high adsorbility. The Bi₂S₃/TiO₂ catalyst shows intense absorption in the visible range due to the narrow bandgap of Bi₂S₃. Under irradiation of solar light, a high efficiency in simultaneously photocatalytic purification of 2,4-dichlorophenoxyacetic acid (2,4-D)/Cr(VI) contaminated water was obtained by employing the Bi₂S₃/TiO₂ NT arrays as photocatalysts. 2,4-D, a stable and toxic aromatic compound, can be effectively decomposed by the hydroxyl radicals initiated by photogenerated holes on the Bi₂S₃/TiO₂ whilst highly poisonous Cr(VI) can be reduced by accepting the electrons and reacting with the byproducts from 2,4-D degradation.

© 2014 Elsevier B.V. All rights reserved.

1. Introduction

Remediation of toxic pollutants in environment by employing photocatalysts has attracted extensive attention in the last few decades [1–3]. Semiconductor based photocatalysts have been widely investigated due to their high efficiency in photocatalysis and solar energy conversion [4,5]. Among the well-known photocatalysts, titanium dioxide (TiO₂) has proven to be the most efficient photocatalyst due to its high photocatalytic capability, chemical stability, non-toxicity, and low cost [6–10]. In a lot of research work, TiO₂ based photocatalysts were in the form of particle, requiring a necessary separation process to remove the TiO₂ particles from the treated wastewater. The separation approaches generally were complex and time consuming [6–10]. In recent years, the application of self-organized TiO₂ NT arrays from the Ti substrate by an anodic oxidation method proved to be an effective approach to avoiding the complex separation steps [11]. Furthermore, compared with TiO₂ particles, the TiO₂ NT

arrays play a more ideal role as catalysts and substrates during photocatalysis by virtue of the high orientation, large internal surface area, controllable mesopore size, as well as eximious electron percolation pathways for vectorial charge transfer and the integrity of the TiO₂ NTs/Ti sheet [11–13].

However, as is known to us, TiO₂ only becomes active under irradiation with ultraviolet (UV) lights due to its high bandgap energy (3.2 eV). Many efforts have been made to extend optical response of TiO₂ into visible light region by doping TiO₂ NT arrays with transition elements to the Ti sites, or N, C, B and S to the oxygen sites, or coupling of TiO₂ with other narrow bandgap semiconductors [11–13].

Since the TiO₂ NT arrays are with good conductivity due to the polarization of TiO₂ in an applied electric field [14], modifying the TiO₂ NT arrays by electrodeposition techniques is with high maneuverability. Bi₂S₃, a narrow bandgap semiconductor (1.28 eV), can be fabricated by electrodeposition, making it possible to deposit Bi₂S₃ crystals on TiO₂ NT arrays directly. The conduction band (CB) of Bi₂S₃ is positioned to a more negative side than that of TiO₂. Irradiated by visible light, Bi₂S₃ is excited, and the photogenerated electrons can be injected into the CB of TiO₂ because the CB level of TiO₂ is lower than that of Bi₂S₃. The electron transfer behavior effectively reduces the probability of light corrosion on Bi₂S₃ and facilitates the separation between

* Corresponding author at: High Level Laboratory of Jiangxi Province for Persistent Pollutants Control, Recycle and Reuse, Nanchang Hangkong University, Nanchang 310063, PR China. Tel.: +86 791 83953373; fax: +86 791 83953373.

E-mail address: sllou@hnu.edu.cn (S. Luo).

the photogenerated holes and electrons of TiO_2 -based catalysts. Although many research work were carried out on the investigation of $\text{Bi}_2\text{S}_3/\text{TiO}_2$ composites [15–17], the white fungus-like mesoporous Bi_2S_3 ball/ TiO_2 NT arrays heterojunctions and the application in photodegradation of 2,4-D have not been reported. In this study, we prepared a new $\text{Bi}_2\text{S}_3/\text{TiO}_2$ composite catalyst with wrinkled mesoporous structure on the TiO_2 NT arrays in hot dimethyl sulfoxide electrolyte through a facile pulsed electrodeposition technique with taking L-cysteine as manipulation molecules. The deposition can be completed in 8 min. The electrodeposited Bi_2S_3 is with high degree of crystallinity due to the fast growth speed provided by the electrodeposition technique [18]. The white fungus-like mesoporous morphology can be attributed to L-cysteine. The as-prepared $\text{Bi}_2\text{S}_3/\text{TiO}_2$ NT arrays can be employed in the simultaneously photocatalytic decontamination of 2,4-dichlorophenoxyacetic acid (2,4-D) and Cr(VI).

The chlorinated aromatic hydrocarbon acid pesticide 2,4-D, is one of the pollutants in water. It was not only used as a common herbicide in the control of broad-leaved weeds and woody plants, but also as an important synthetic auxin in laboratories for plant research [19]. As a widely used reagent, 2,4-D has much potential environmental harmfulness such as teratogenicity, carcinogenicity and mutagenicity. Because of the high stability of 2,4-D, 2,4-D was generally oxidized to harmless carbonate compounds by the photogenerated holes from excited TiO_2 based catalysts under UV light and assisted by microwave or $\text{Fe}^{2+}/\text{H}_2\text{O}_2$ [20–22]. On the other hand, as a significant environmental contaminant, Cr(VI) can cause a series of toxicological effects on human and ecological environment. Cr(VI) is usually derived from various industrial operations, including metallurgy, chemical manufacturing, leather tanning, electroplating, metal corrosion, and pulp production [23–26]. The highly toxic Cr(VI) can be reduced by photogenerated electrons generated on TiO_2 to trivalent chromium (Cr(III)) with much lower toxicity and limited hydroxide solubility [27]. Since herbicides and heavy metal ions often coexist in real wastewaters, investigating the influence of mutual interactions on the photocatalytic conversion process will be of great importance in the field of environmental recovery.

In this work, 2,4-D and Cr(VI) were selected as the deputies of herbicides and heavy metal ions respectively. The simultaneous and synergistic photocatalytic oxidation of 2,4-D and reduction of Cr(VI) was investigated in presence of wrinkled mesoporous $\text{Bi}_2\text{S}_3/\text{TiO}_2$ hybrid photocatalyst. In this photocatalysis, 2,4-D served as the photogenerated holes scavenger and was oxidized, while Cr(VI) mainly acted as photogenerated electrons acceptor and was reduced. Consequently, it is expected to reach an excellent synergistic detoxification effect between 2,4-D and Cr(VI).

2. Experimental

2.1. Materials

Titanium foils (127 μm thick, 99.8%) were purchased from Sigma-Aldrich, America. Dimethyl sulfoxide (DMSO), HF, sulfur powder, bismuth nitrate pentahydrate and L-cysteine were analytical reagents. Methanol and phosphate were HPLC grade, purchased from Tedia Company, USA. All the other reagents were analytical grade purity, and were used as received without further purification. Milli-Q water was used throughout this study.

2.2. Fabrication of $\text{Bi}_2\text{S}_3/\text{TiO}_2$ NT arrays

TiO_2 NT arrays were prepared by electrochemical anodization with a DC power (Array 3646A, Taiwan, China). After being ultrasonically cleaned in acetone, isopropanol and ethanol, titanium foil (geometrical size: 3 cm \times 1 cm) was anodized at 30 V for

10 h in a nonaqueous electrolyte, 2 wt% HF in DMSO solution. All anodizations were carried out at 25 °C using a two-electrode electrochemical cell with a Pt counter electrode.

Bi_2S_3 crystal was synthesized on TiO_2 NT arrays with the electrochemical workstation (CHI660 C, Shanghai, China). Prior to Bi_2S_3 deposition, the as-anodized TiO_2 NT arrays were sintered at 500 °C for 4 h with a heating rate of 2 °C min^{−1} in a unsealed tube furnace (SK2-15, Changsha, China). The electrodeposition experiment was carried out as follows: 0.1 mol/L sulfur powder and 0.06 mol/L bismuth nitrate pentahydrate were dissolved into 20 ml of DMSO solution in turn under stirring and heat. After S and $\text{Bi}(\text{NO}_3)_3$ were totally dissolved, 0.12 mol/L L-cysteine was added into the solution to serve as manipulation molecule during the growth process of Bi_2S_3 clusters.

The electrochemical deposition was performed in a three-electrode system with the TiO_2 NTs/Ti, a platinum wire, and a saturated calomel electrode (SCE) serving as working electrode, auxiliary electrode and reference electrode, respectively. Bi_2S_3 clusters were prepared by applying a rectangular potential pulsed mode.

For pulsed electrodeposition, during each pulse, a potential of −2.0 V was applied for 0.2 s, followed by a potential of −0.0001 V being applied for 1 s under 125 °C. The number of consecutive pulse sequence was 400. The pulsed electrodeposition maximum current is 5.7×10^{-2} A/cm². After the electrodeposition, the as-prepared $\text{Bi}_2\text{S}_3/\text{TiO}_2$ NT arrays was washed several times by anhydrous ethanol and dried in air.

2.3. Characterization and optical determination of $\text{Bi}_2\text{S}_3/\text{TiO}_2$ NT arrays

The morphologies of the resulting $\text{Bi}_2\text{S}_3/\text{TiO}_2$ NT arrays were characterized by a field emission scanning electron microscopy (FESEM, Hitachi-4800, Japan). Transmission electron microscopy (TEM) images were obtained using a JEM 3010 (JEOL, Tokyo, Japan) operating at 300 kV. The crystal structure of the catalyst was investigated using the X-ray diffractometer (XRD, M21X, MAC Science Ltd., Japan) with Cu K α radiation ($\lambda = 0.15406$ nm). UV-visible absorption spectra of the specimens were recorded with a Varian Cary 300 spectrometer equipped with an integrating sphere ($R = 150$ mm).

2.4. Photocatalysis on $\text{Bi}_2\text{S}_3/\text{TiO}_2$ NT arrays and analytical procedures

The simultaneous photocatalytic removal of Cr(VI) and 2,4-D by $\text{Bi}_2\text{S}_3/\text{TiO}_2$ NTs was performed in a photochemical reactor. The composite catalyst with effective geometrical area of 2.7 cm² was placed in the solution containing Cr(VI) and 2,4-D which concentration are both 10 mg L^{−1}. A xenon lamp (CHF-XM35-500 W, Beijing Trusttech. Co. Ltd.) was served as the light source with a radiation intensity of 85 mW/cm² measured by a radiometer (OPHIR, Newport, USA). The concentration of 2,4-D was determined by recording the absorbance of sample solution at 284 nm using UV-vis spectrophotometer (Cary 300, USA). While Cr(VI) was determined colorimetrically at 540 nm according to the diphenylcarbazide colorimetric method (GB 7466-87, Standards of China). To monitor the mineralization of 2,4-D, total organic carbon (TOC) was measured using a Shimadzu TOC VCSN analyzer. The TOC concentration includes the carbon content of the target compound, the oxalate and the intermediates generated during the experiment. The pH of 2,4-D/Cr(VI) coexisting aqueous solution was determined by a Delta 320 pH meter (Mettler-Toledo, Shanghai, China). The identification and quantification of the major resulting products were carried out by a high-performance liquid chromatograph (HPLC-WATERS 2695) equipped with a C18 column (25 cm \times 4.6 mm,

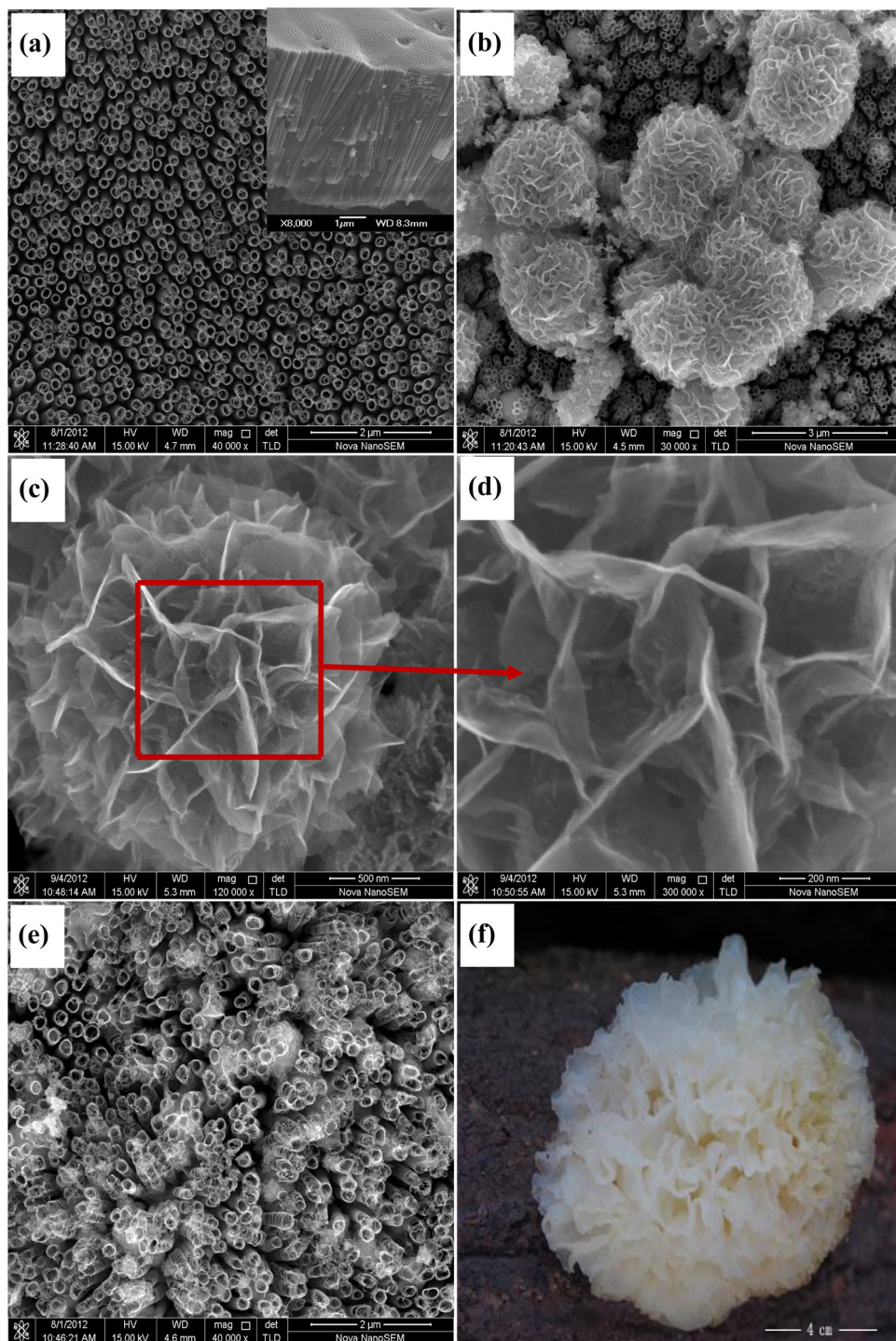


Fig. 1. (a) SEM images of the top surface and cross section of the TiO₂ NT arrays; (b) SEM image showing morphologies of prepared Bi₂S₃ balls/TiO₂ NT arrays under low magnification; (c) and (d) SEM images showing the detail mesoporous character of the Bi₂S₃ ball; (e) SEM image of the TiO₂ NT arrays with Bi₂S₃ crystals in between them; (f) a typical picture showing a white fungus.

5 μm) and a UV detector ($\lambda = 284$ nm) with methanol-phosphate (60:40 (v/v)) mobile phase. The intermediate products was determined by Xevo G2 QT of Mass spectrometer (MS, Xevo G2 QT of, Waters, America). The MS conditions were list as follows: capillary voltage was 2.5 kV in negative mode, sampling cone voltage was 45 V, desolvation temperature was 250 °C, desolvation gas flow was 600 L/h.

All the aforementioned analyses were carried out on a minimum number of three replicate samples and the average values were reported.

3. Results and discussion

3.1. Morphology and structural characterization of Bi₂S₃/TiO₂ NT arrays

The SEM images of the as-prepared TiO₂ nanotube arrays and Bi₂S₃/TiO₂ composite nanotube arrays are shown in Fig. 1. As Fig. 1a shows, the unmodified TiO₂ NT arrays with 6.5 μm in length (shown as the inset), 110 nm in pore size, and 15 nm in wall thickness are arranged uniformly and compactly. After the

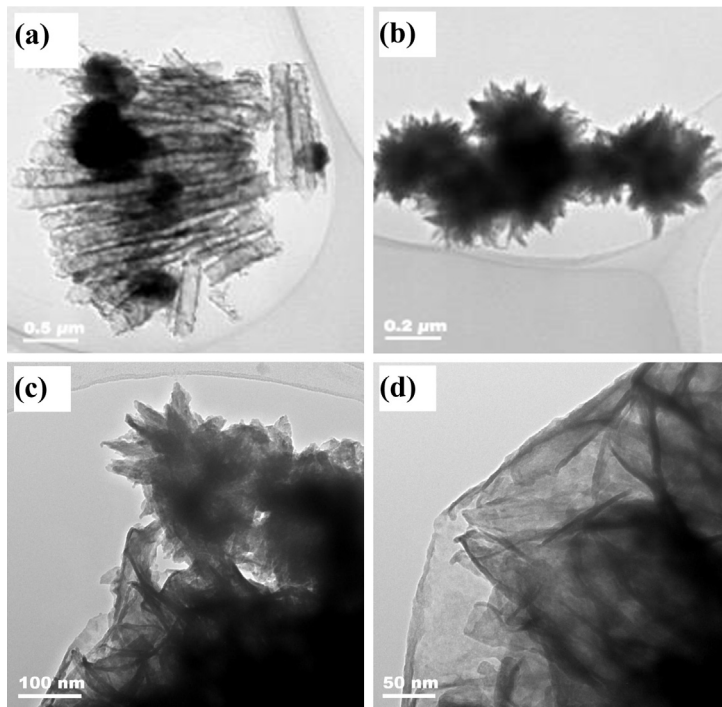


Fig. 2. TEM images of (a) $\text{Bi}_2\text{S}_3/\text{TiO}_2$ nanotubes, (b) mesoporous Bi_2S_3 balls, (c) and (d) high resolution TEM images of Bi_2S_3 .

electrodeposition, a lot of Bi_2S_3 balls with wrinkled surface are dispersed on the TiO_2 NT arrays top surface. As the plots in Fig. 1c and d show, the white fungus-like, mesoporous structure consists of interconnected Bi_2S_3 crystal sheets with 5 nm in thickness, 100–200 nm in pore size. The mesopores distribute all over the Bi_2S_3 balls, suggesting a prospect of high adsorbility. Furthermore, the relatively large, connected and regular pores are more favorable than randomly formed inaccessible narrow pores during the transfers of a media [28]. Except the mesoporous Bi_2S_3 balls on the top surface, Bi_2S_3 crystals can also be deposited in between the TiO_2 NTs, shown as Fig. 1e. Compared with the unmodified TiO_2 NT arrays, the as-prepared $\text{Bi}_2\text{S}_3/\text{TiO}_2$ composite NT arrays with unique physical structure have sharp corners and edges, large surface area and a better adsorption capacity, which can significantly improve the photocatalytic efficiency in the practical application. Observed under low magnification, the Bi_2S_3 balls look like white funguses (Fig. 1f) which can be attributed to the introduction of the

L-cysteine. This is due to the inhibiting effect of the typical growth of Bi_2S_3 along c axis by the coordination of the functional groups of L-cysteine such as $-\text{NH}_2$, $-\text{SH}$, $-\text{OH}$ to Bi^{3+} . At the same time, extended growth along a-b plane of Bi_2S_3 is promoted which results in the formation of the funguses mesoporous Bi_2S_3 balls [18].

TEM images of the $\text{Bi}_2\text{S}_3/\text{TiO}_2$ NT arrays are shown in Fig. 2. Fig. 2a is the TEM image of $\text{Bi}_2\text{S}_3/\text{TiO}_2$ nanotubes, showing that some Bi_2S_3 balls are attached on the TiO_2 NTs. Fig. 2b shows that the white fungus-like mesoporous Bi_2S_3 balls have sharp edges which can serve as active sites during the photocatalytic reactions. The high-magnified TEM images in Fig. 2c and d depict the multilayer Bi_2S_3 with crinkle textures.

As is known to us, the crystal structure of TiO_2 greatly affects its photocatalytic activity. Therefore, the crystalline phase of $\text{Bi}_2\text{S}_3/\text{TiO}_2$ nanotube arrays was investigated by XRD. As the XRD pattern in Fig. 3a shows, sharp reflections marked by square are assigned to the orthorhombic Bi_2S_3 . Detail indexes of the crystal

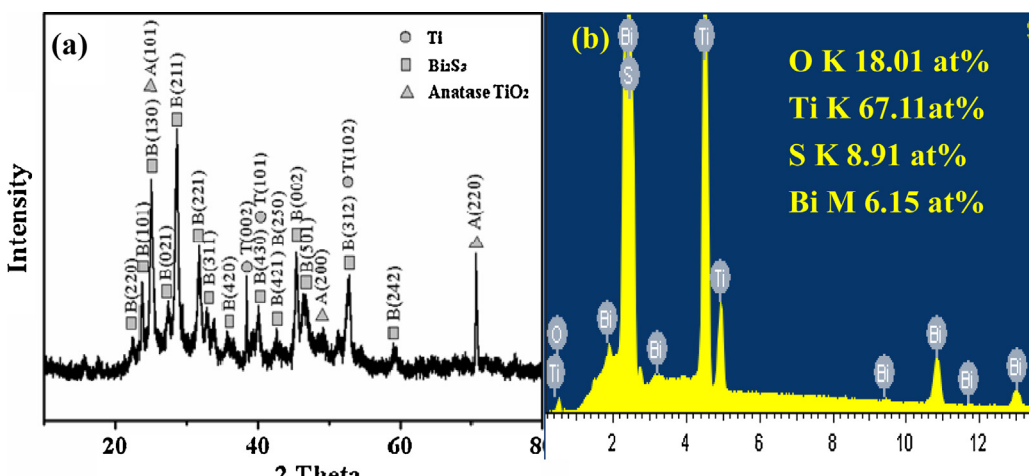


Fig. 3. (a) XRD pattern and (b) EDS spectrum of $\text{Bi}_2\text{S}_3/\text{TiO}_2$ samples. The typical crystal lattice indexes of orthorhombic Bi_2S_3 are labeled in (a).

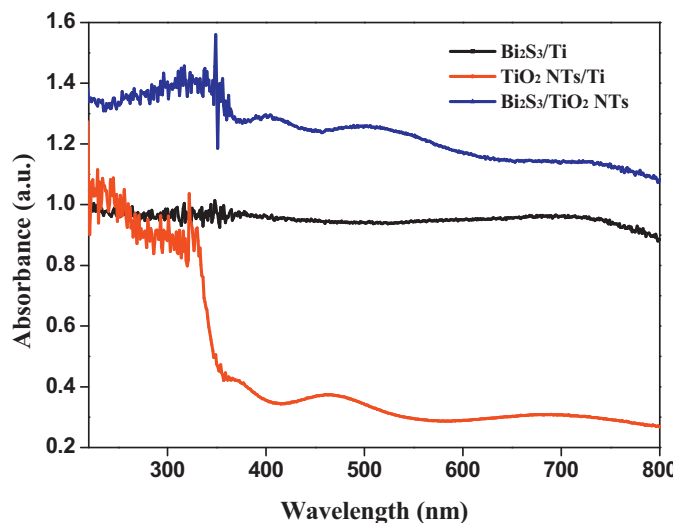


Fig. 4. UV-vis spectra of the Bi₂S₃/TiO₂ NT arrays, unmodified TiO₂ NT arrays, and Bi₂S₃ crystals.

lattice are labeled. The crystallization phase of TiO₂ detected in the sample is anatase which is considered to have a higher photocatalytic activity than that of rutile and brookite. The remaining peaks are assigned to the Ti substrate. The energy dispersive spectroscopy (EDS) spectrum in Fig. 3b shows the signals of Bi, S as well as those of Ti and O elements. The corresponding element analysis embedded in the EDS panel illustrates that the atom ratio of Bi:S is 1.95:3.01, suggesting that the Bi₂S₃ crystal is with high stoichiometric ratio.

The UV-vis absorption spectrum of TiO₂ NTs in Fig. 4 displays no significantly optical absorption in the visible region except the slight absorption at 480 nm. The oxygen defects/vacancies generated in anodization of TiO₂ NTs are responsible for the tiny response in the visible [29]. Bi₂S₃/TiO₂ NTs exhibit strong spectral response in both the UV and the visible region. That is the effect of the narrow bandgap of Bi₂S₃ (1.28 eV). The improved light absorption can therefore excite more photogenerated carriers from the Bi₂S₃/TiO₂ NTs to decontaminate the pollutants, which would improve the practical application under natural solar light. Increasing the number of consecutive pulse sequence to 1200, TiO₂ NT arrays were totally covered by Bi₂S₃ crystals. The corresponding SEM image under low magnification was provided in Fig. A1 as supplementary data. Since TiO₂ was shielded, it is reasonable to ascribe the optical absorption to Bi₂S₃. The Bi₂S₃ crystals exhibit a color of black, resulting in a total absorption in the light range of 200–800 nm, shown as Fig. 4.

3.2. Adsorption capacity and photocatalytic activity of the photocatalysts

The absorption capacities of target catalysts were evaluated by adsorption experiments. The adsorption experiments of Cr(VI) and 2,4-D were carried out with a 25 mL 5 mg L⁻¹ Cr(VI) and 5 mg L⁻¹ 2,4-D solution in dark for 2 h on different photocatalysts. Fig. 5a depicts absorption capacities of Bi₂S₃ crystals, TiO₂ NTs, and Bi₂S₃/TiO₂ heterojunctions toward 2,4-D and Cr(VI). The absorption rates in dark toward 2,4-D over Bi₂S₃ crystals, TiO₂ NTs, and Bi₂S₃/TiO₂ NTs were 4%, 1.2%, and 4.5%, respectively. The absorption rates toward Cr(VI) over the three catalysts were 5.2%, 2.8%, and 7.2%, respectively. Bi₂S₃/TiO₂ NTs show the highest absorption capacity toward 2,4-D and Cr(VI), which can be attributed to the 3D mesoporous structure of Bi₂S₃ balls. TiO₂ NTs did not exhibit high uptake as Bi₂S₃. It is considered that the capillary actions of NTs hinder the infiltration of the pollutants.

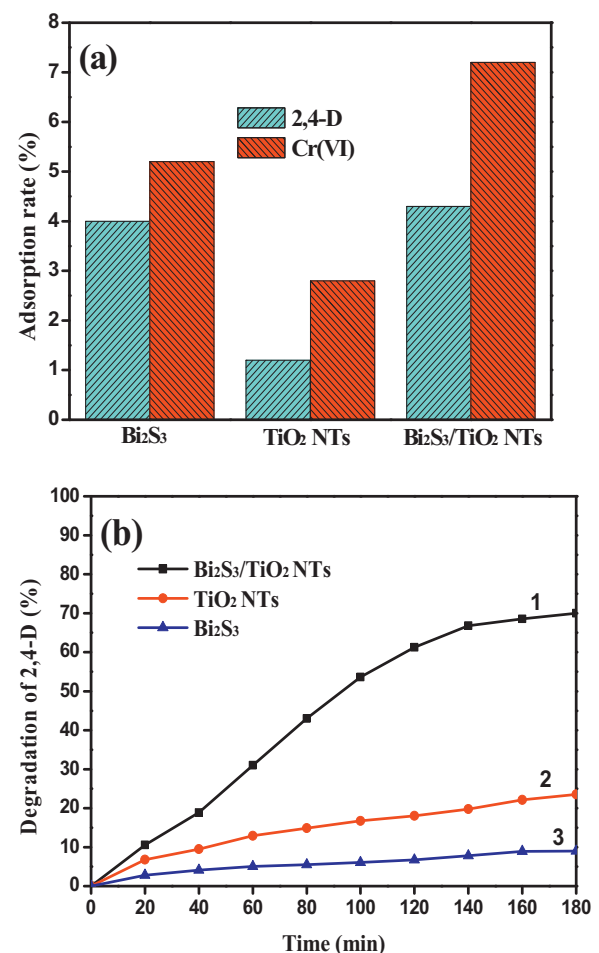


Fig. 5. (a) Absorption rate of 2,4-D and Cr(VI) over Bi₂S₃/TiO₂ NTs, unmodified TiO₂ NTs, and Bi₂S₃ crystals, (b) degradation efficiencies of 2,4-D over Bi₂S₃/TiO₂ NTs, unmodified TiO₂ NTs, and Bi₂S₃ crystals under simulated solar light $V_{\text{total}} = 60 \text{ mL}$, $S_{\text{catalyst}} = 2.7 \text{ cm}^2$, light source: Xe lamp, 85 mW/cm².

Degradation efficiencies of 60 mL 2,4-D (10 mg L⁻¹) in 180 min on Bi₂S₃/TiO₂ NTs, pristine TiO₂ NTs, and Bi₂S₃ crystals were compared in Fig. 5b. The Real-time UV-vis spectra of 2,4-D water sample with initial pH 4.0 in the presence of Bi₂S₃/TiO₂ NTs were supplied in Fig. A2 as supplementary data. As Fig. 5b shows, the degradation rate of 2,4-D on Bi₂S₃/TiO₂ NTs (curve 1) is 14.8 $\mu\text{g/L min cm}^2$ which is about three times that of the unmodified TiO₂ NTs (curve 2) and more than seven times that on Bi₂S₃ crystals (curve 3). Since CB of TiO₂ is more anodic than CB of Bi₂S₃, and VB of Bi₂S₃ is more cathodic than VB of TiO₂, under illumination, the electrons excited on Bi₂S₃ CB would transfer to TiO₂ CB, whereas the holes generated on TiO₂ VB would transfer to Bi₂S₃ VB. The transfer behaviors of the electrons and holes can reduce the recombination probability between them by carrying out reduction and oxidation processes in different regions, which results in the highest catalytic activity of Bi₂S₃/TiO₂ NTs.

3.3. Simultaneous detoxification of 2,4-D and Cr(VI) by Bi₂S₃/TiO₂ NTs and influence of Bi₂S₃ and TiO₂

It is known that the key point in photocatalytic applications is to inhibit the recombination of photogenerated electron-hole pairs and improve the utilization efficiency of light quantum. As mentioned above, photocatalytic oxidation of 2,4-D needs to consume photogenerated holes while photocatalytic reduction of Cr(VI) needs to accept the photogenerated electrons. In addition,

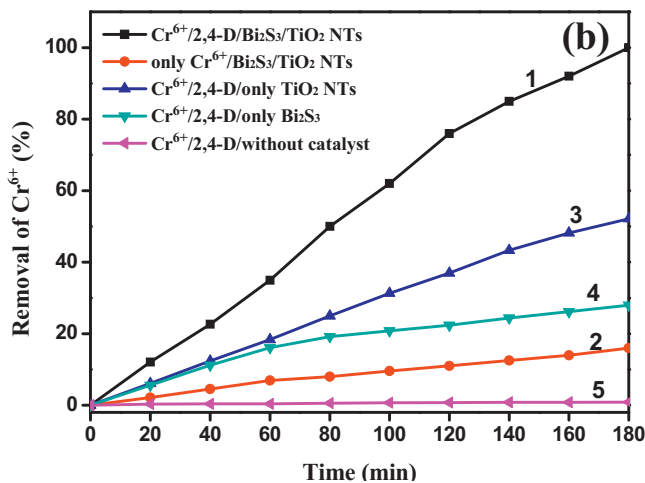
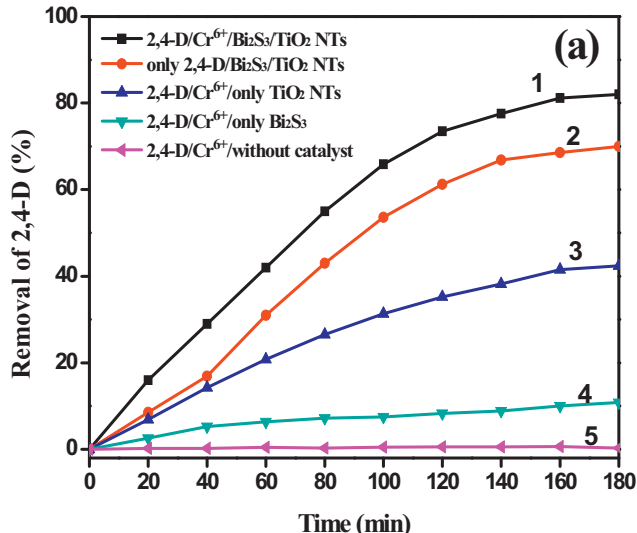


Fig. 6. (a) Photocatalytic degradation efficiencies of 2,4-D in absence/presence of Cr(VI) on Bi₂S₃/TiO₂ NTs, unmodified TiO₂ NTs, and Bi₂S₃ crystals, (b) photocatalytic reduction of Cr(VI) to Cr(III) in absence/presence of 2,4-D on Bi₂S₃/TiO₂ NTs, unmodified TiO₂ NTs, and Bi₂S₃ crystals. ^aV_{total} = 60 mL, S_{catalyst} = 2.7 cm², light source: Xe lamp, 85 mW/cm².

Cr(VI) is an oxidant under acidic conditions which can assist the degradation of 2,4-D. Therefore, it is expected to achieve an ideally simultaneous detoxification of 2,4-D and Cr(VI).

In this study, a 60 mL simulated wastewater with pH of 4.0, containing 10 mg L⁻¹ 2,4-D and/or 10 mg L⁻¹ Cr(VI) was purified under variable conditions within 180 min.

Detoxification efficiencies of 2,4-D in controlled experiments are shown in Fig. 6a. 2,4-D removal efficiency (RE) in coexisting system is 81% over Bi₂S₃/TiO₂ NTs (curve 1) and 71% without Cr(VI) in solution (curve 2). Related degradation rates are 14.8 and 16.3 µg/L min cm², respectively. The RE on TiO₂ NTs (curve 3) is 42.4%. The modification of Bi₂S₃ increases RE by 38.6%. If there is no TiO₂, the RE over pristine Bi₂S₃ crystals is only 10.9% (curve 4), suggesting the combination of TiO₂ in photocatalysis is necessary. As curve 5 shows, 2,4-D was hardly degraded in the absence of photocatalysts, even assisted by Cr(VI), suggesting that 2,4-D cannot be oxidized by Cr(VI) directly. Simultaneously, fast and complete reduction of Cr(VI) was achieved in the coexisting system with a reducing rate of 20.6 µg/L min cm², shown as curve 1 in Fig. 6b. In the absence of 2,4-D, the reduction of Cr(VI) is very slow (Fig. 6b, curve 2) because of a continuous reduction and reoxidation

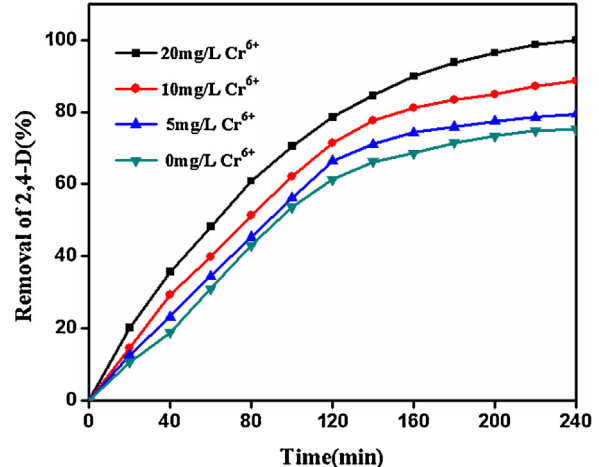


Fig. 7. Influence of initial Cr(VI) concentration on the photocatalytic degradation rate of 2,4-D. ^aV_{total} = 60 mL, S_{catalyst} = 2.7 cm², light source: Xe lamp, 85 mW/cm².

of chromium species by the photogenerated holes and hydroxyl radicals. 2,4-D plays a key role by acting as a scavenger to deplete the holes during the Cr(VI) reduction process. The removal efficiencies of Cr(VI) are 51.3% and 28% over pristine TiO₂ NTs (curve 3) and Bi₂S₃ crystals (curve 4), respectively. In addition, no reduction happens on Cr(VI) in the absence of photocatalysts (curve 5 in Fig. 6b), confirming that Cr(VI) is reduced by photogenerated electrons. Comparing plots a and b in Fig. 6, the removal efficiencies of Cr(VI) are higher than those of 2,4-D under same conditions. That is because it is simple for Cr(VI) to accept the photogenerated electrons to be reduced. However, photocatalytic degradation of 2,4-D suffers a complex procedure to remove the substituents and destroy the benzene ring. Much more radicals are needed to deplete the intermediates to species with small molecular weights.

3.3.1. Influence of initial concentration of Cr(VI) on the degradation of 2,4-D

The influence of initial concentration of Cr(VI) on the removal of 10 mg L⁻¹ 2,4-D was studied by increasing the Cr(VI) concentration from 0 to 20 mg L⁻¹ at pH 4.0. As shown in Fig. 7, with the increasing of the initial concentration of Cr(VI), the removal efficiency of 2,4-D increased accordingly. Moreover more photogenerated electrons were consumed by more Cr(VI) ions, which contributes to the generation of more holes for the oxidation of 2,4-D. In addition, a faster oxidizing speed can be devoted by Cr(VI) by reacting with the organic acid with low molecular weight generated from 2,4-D degradation [30,31]. 2,4-D was totally degraded in the presence of 20 mg L⁻¹ Cr(VI) after 240 min irradiation.

3.3.2. pH Influence on the removal of Cr(VI) and 2,4-D

Fig. 8 displays the pH effect (adjusted by H₂SO₄ or NaOH) on the removal efficiencies of 2,4-D and Cr(VI) in the coexisting system containing 10 mg L⁻¹ 2,4-D and 10 mg L⁻¹ Cr(VI). Since Cr(VI) is only reduced under acidic condition, the pH value was adjusted to 1, 3, 4 and 5. In Fig. 8a, with the increasing of the pH, the photoreduction rate of Cr(VI) decreased noticeably, with the calculated value of 26.5, 23.7, 22.4, and 18.6 µg/L min cm² at pH 1.0, 3.0, 4.0, and 5.0, respectively. The reduction of Cr(VI) increases with the increased acidity of the water sample. That is because the oxidizing capacity of Cr(VI) increases with the increased H⁺ concentration, which accelerates the chemical reaction rate between Cr(VI) and the byproducts from 2,4-D degradation [13,30,31]. As a result, the reduction of Cr(VI) is accelerated. Cr(VI) is totally reduced after being irradiated for 140 min at pH 1.0 in the presence of 2,4-D.

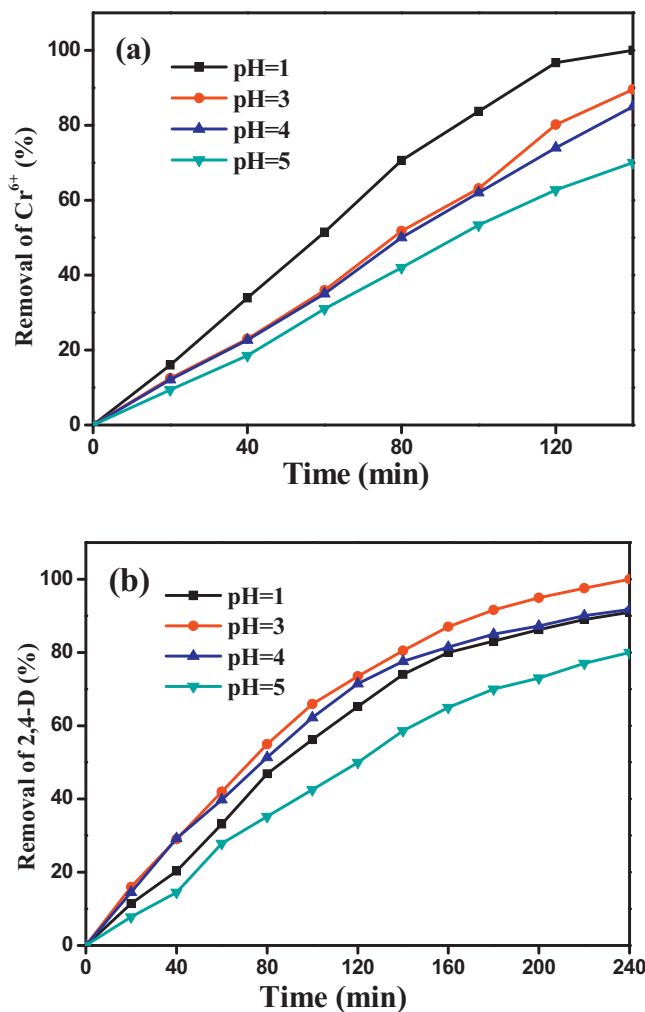


Fig. 8. Influence of pH on photocatalytic reduction rate of Cr(VI) (a) and photocatalytic degradation rate of 2,4-D, (b) ^aV_{total} = 60 mL, S_{catalyst} = 2.7 cm², light source: Xe lamp, 85 mW/cm².

The pH value not only exhibits important influence on oxidation potential and surface charge of the catalyst but also affects their adsorption and dissociation of 2,4-D, which determines the final catalysis efficiency. The pKa value of 2,4-D is 2.83. When pH value is higher than 2.83, 2,4-D mainly exists as anion. Conversely, 2,4-D exists mainly in the form of acid. The zero point charge (zpc) pH_{zpc} for Bi₂S₃/TiO₂ NTs is 7.36 (Supplementary data: Fig. A3). When pH < 7.36, the catalyst surface is positively charged. So in the pH range of 2.83–7.36, there are electrostatic interactions between the positive catalyst surface and negative 2,4-D anions which results in a strong adsorption between the Bi₂S₃/TiO₂ NT surface and 2,4-D. As Fig. 8b shows, the degradation rate of 2,4-D at pH 1, 3, 4, and 5 is 49.5, 55.6, 49.9, and 44.4 µg/L min cm², respectively. The highest degradation efficiency of 2,4-D was achieved at pH 3 but not 1, 4 or 5. This can be explained that hydroxyl radicals are the key factors for the oxidation of 2,4-D. In strong acidic medium of pH = 1, the OH⁻ concentration is so low that it is unfavorable for the formation of hydroxyl radicals. Furthermore, 2,4-D is mainly in form of acid at pH = 1, which is positively charged. Bi₂S₃/TiO₂ NT surface is unfavorable for the absorbing of the positively charged acid form of 2,4-D, which reduces the reaction possibility. The zeta potential is 23.9, 9.6, and 4.2 mV for Bi₂S₃/TiO₂ NT at pH = 3, 4, and 5, respectively. The adsorption of 2,4-D on Bi₂S₃/TiO₂ NT at pH 3 is much stronger than that at pH 4 and 5. A high zeta potential of the photocatalyst surface indicates a high electrostatic attraction

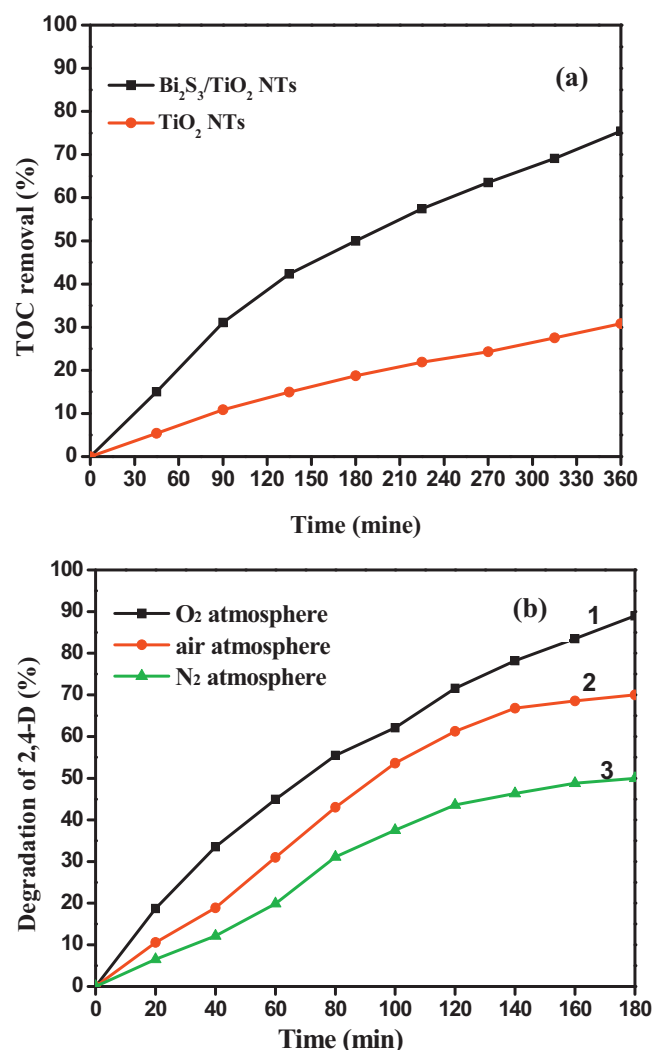


Fig. 9. (a) TOC removal efficiencies of 2,4-D assisted by Bi₂S₃/TiO₂ NTs and TiO₂ NTs, (b) degradation efficiencies of 2,4-D in O₂, air, and N₂ atmosphere ^aV_{total} = 60 mL, S_{catalyst} = 2.7 cm², light source: Xe lamp, 85 mW/cm².

and a high adsorbility toward the organic pollutant. This explains why the highest catalytic efficiency was obtained at pH 3. All things considered, 3 is the optimum pH value for purifying the complexed 2,4-D/Cr(VI) water.

3.3.3. Photocatalytic mechanism on Bi₂S₃/TiO₂ NTs and analyses of intermediate degradation products

2,4-D is a very stable organic pollutant. In order to estimate the mineralization degree of 2,4-D, total organic carbon (TOC) of the 2,4-D/Cr(VI) solution was determined during the photocatalysis. Fig. 9a illustrates the TOC data in dependence on the irradiation time during the degradation of 2,4-D. As the curves show, removal efficiency analyzed by TOC for 2,4-D on Bi₂S₃/TiO₂ NTs is higher than that on TiO₂ NTs which indicates a high catalytic activity of Bi₂S₃/TiO₂ NTs on the mineralization of 2,4-D.

As is known, water and oxygen molecules are necessary for the photooxidation process. Besides the reaction between holes and absorbed water, hydroxyl radicals can also be generated through the reaction between dissolved oxygen and the photogenerated electrons in excited semiconductor [32]. Our experiments were carried out with being exposed to air. Controlled photocatalytic detoxifications of 2,4-D with the solution being bubbled by O₂, and N₂ were performed to clarify the degradation mechanism of 2,4-D

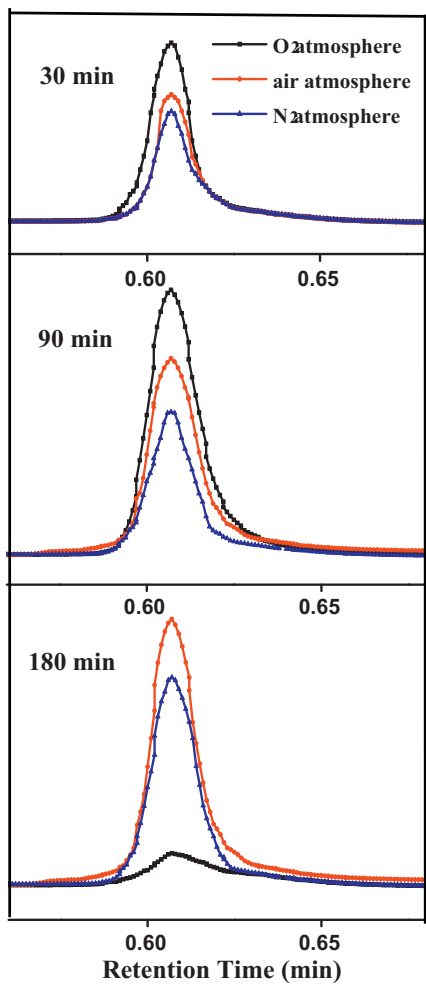
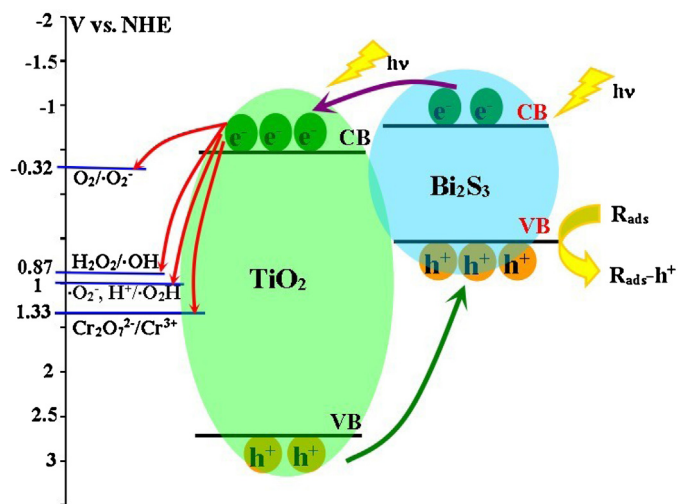


Fig. 10. HPLC chromatograms of benzoquinone during the photocatalytic degradation of 2,4-D in O_2 , air, and N_2 atmosphere.

in this work. As Fig. 9b shows, the removal efficiencies of 2,4-D in O_2 , air, and N_2 atmosphere in 180 min are 89.7%, 71%, and 49.6% respectively. The fast degradation rate was achieved in O_2 atmosphere. However, in N_2 atmosphere, the dissolved O_2 was released by N_2 bubbles, the yield of $\cdot O_2^-$ declined, and therefore the generation of $\cdot OH$ was decreased, which results in the degradation efficiency of 2,4-D decrease from 71% in air to 49.6% in N_2 atmosphere. The above results suggest that the dissolved oxygen is the key factor to realize the degradation of 2,4-D over Bi_2S_3/TiO_2 catalyst.

Fig. 10 shows the HPLC chromatograms of benzoquinone generated during the degradation of 2,4-D in O_2 , air, and N_2 atmosphere. As shown, benzoquinone with the highest yield was determined in the solution bubbled by O_2 after 30 min. The amount of benzoquinone is lowest in N_2 atmosphere because the dissolved oxygen was released by N_2 bubbles. All the amounts under the three occasions are much higher at 90 min than those at 30 min, which suggests the continuous generation of benzoquinone. With the evolution of photocatalytic degradation, the benzoquinone was consumed by the hydroxyl radicals. At 180 min, the lowest amount of benzoquinone is obtained in O_2 atmosphere while the highest is observed in N_2 atmosphere. The results indicate that high oxygen concentration is favorable for the generation of benzoquinone from hydroquinone in initial stage. After reaching a maximum, benzoquinone can then be oxidized by hydroxyl radicals. The depleting rate depends on the density of O_2 in the solution. The mass spectra of benzoquinone was supplied as Fig. A4.

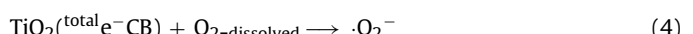
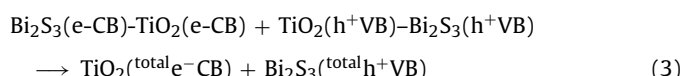
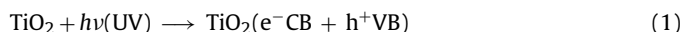


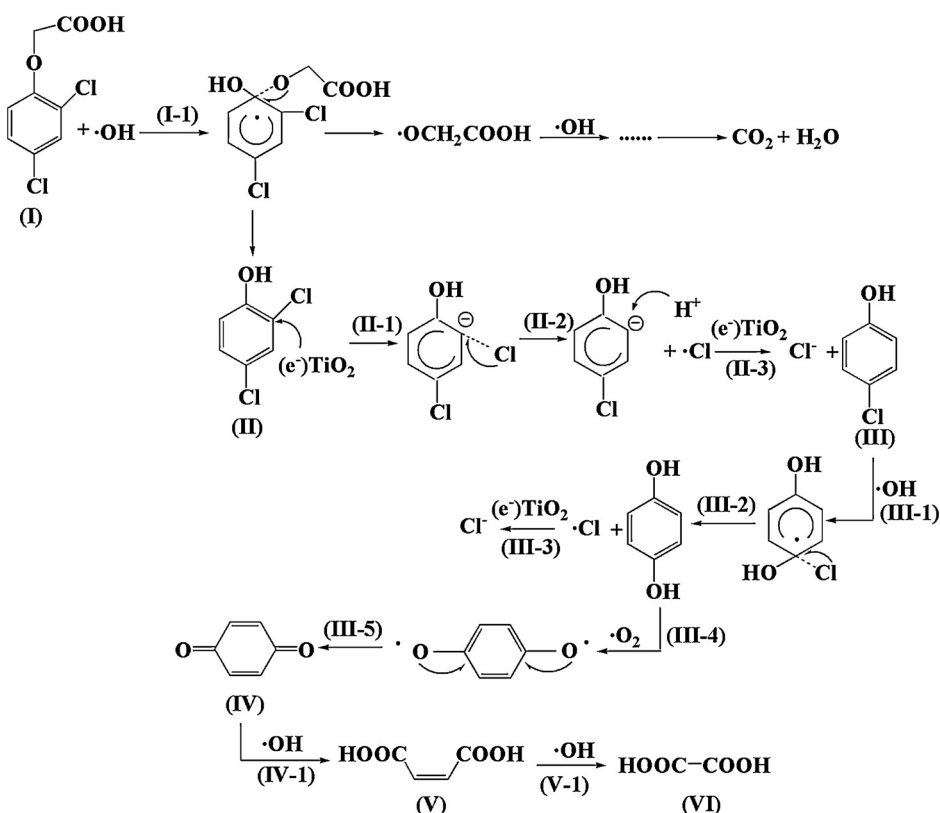
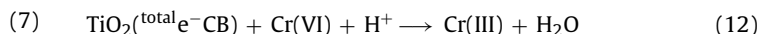
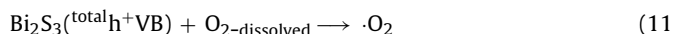
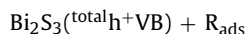
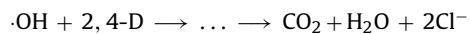
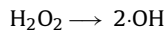
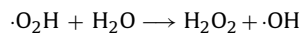
Scheme 1. Energetic diagrams illustrating the transfer behaviors of the photogenerated holes and electrons in Bi_2S_3/TiO_2 junction interface.

In the light of the experiment results and by referring to the literatures [32–34], the transfer behaviors of the photogenerated holes and electrons in Bi_2S_3/TiO_2 heterojunctions are illustrated in Scheme 1. As shown, the CB and VB of Bi_2S_3 lie above those of TiO_2 . Under irradiation, the electrons excited in Bi_2S_3 CB would transfer to TiO_2 , whereas the holes generated in TiO_2 VB prefer opposite transfer to that of Bi_2S_3 . The electrons in TiO_2 CB are rapidly delivered to adsorbed oxygen to produce $\cdot O_2^-$, which can generate hydroxyl radicals by reacting with H_2O . The produced hydroxyl radicals are determinable to oxidize 2,4-D. Simultaneously, Cr(VI) converts to Cr(III) by accepting the electrons. Holes in Bi_2S_3 VB induce oxidation with surface adsorbed species to favoring the degradation of 2,4-D.

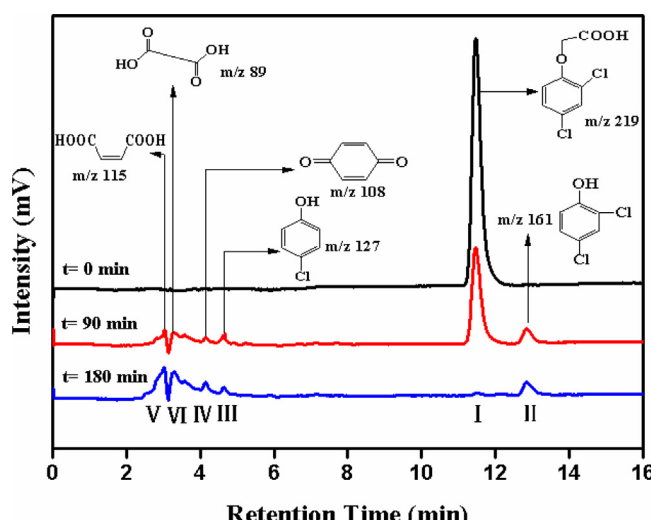
Furthermore, the highly orientated TiO_2 NT arrays are good pathway for the electron transfer. Consequently, the effective separation of the h-e pairs at Bi_2S_3/TiO_2 heterojunctions can be realized, which reduces the recombination chance of h-e pair and increases the quantum efficiencies. 2,4-D can be degraded by the hydroxyl radicals initiated by the holes and Cr(VI) can be reduced by the electrons.

Although the characteristic peak of 2,4-D in UV-vis spectra (Fig. A2) almost disappeared after being treated for 180 min, the TOC value (Fig. 9a) shows a reduction of 52% with Bi_2S_3/TiO_2 NTs over the 180 min treatment, indicating that byproducts were formed due to an incomplete oxidation of 2,4-D. The intermediate products from the degradation process of 2,4-D and corresponding structural formulas were identified by HPLC-MS and are labeled in Fig. 11. Based on the HPLC and MS results, the detail photocatalytic reactions occurred on Bi_2S_3/TiO_2 NTs can be expressed by Eqs.(1)–(12). The degradation pathway of 2,4-D is illustrated in Scheme 2.



**Scheme 2.** Producing pathway of the intermediate degradation products of 2,4-D.

In Fig. 11, the chromatogram at 180 min shows that the characteristic peak assigned to 2,4-D (I) disappears while the peaks attributed to the intermediate products still exist. That is the reason the TOC removal efficiency is 52% at 180 min. Illustrated as Scheme 2, the initial reactions were performed between 2,4-D and hydroxyl radicals generated in Eqs. (7) and (8). Based on the locating regularity of the substituent on the benzene ring, it is preferable for ·OH to attack the carbon atom where is –OCH₂COOH substituting (reaction I-1 in Scheme 2), which generates a main by-product of 2,4-dichlorophenol (II, 2,4-DCP). As shown in Scheme 2, the electrophilic attack from the photogenerated electrons in TiO₂ CB (Eq. (3)) happens on the position with a chloride substituent affected by a hydroxyl at its ortho-position and another chloride substituent at its meta-position (reaction II-1), generating *p*-chloramphenicol anion (reaction II-2). Then *p*-chlorophenol (III) and chloride are formed by reacting with hydrogen ions and e[–]_{CB}, respectively [30,31]. In reaction III-1, III-2, the electro-donor property of hydroxyl group on the benzene of *p*-chlorophenol (III) facilitates the attack of ·OH onto the para-position, leading to the final formation of hydroquinone. In reaction III-4, the hydroquinone undergoes reaction with the oxygen radical generated in Eq. (11), producing benzoquinone (IV). Comparing the HPLC chromatograms obtained at 90 min and 180 min, there is an obvious decrease of peak III and an increase of peak IV, suggesting the consumption of *p*-chlorophenol and the production of benzoquinone. Then aromatic ring is broke by ·OH, producing maleic acid (V) in reaction IV-1. The maleic acid is further oxidized to oxalic acid (VI) in Fig. 11 by ·OH (reaction V-1). Finally, the oxalic acid can be oxidized by ·OH and Cr(VI) to carbon dioxide.

**Fig. 11.** Evolution of HPLC chromatograms during the degradation of 2,4-D.

4. Conclusions

White fungus-like mesoporous Bi_2S_3 balls modified TiO_2 nanotube arrays were successfully prepared by a simple pulsed electrodeposition technique. The as-prepared wrinkled mesoporous Bi_2S_3 balls consist of connected and regular pores with 100–200 nm in pore size and 5 nm in wall thickness. The resulting $\text{Bi}_2\text{S}_3/\text{TiO}_2$ nanotube arrays showed much higher adsorption capacity and photocatalytic activity under visible light irradiation than the unmodified TiO_2 due to the mesoporous property of narrow bandgap Bi_2S_3 balls. In the simultaneous detoxification of 2,4-D and Cr(VI) employing $\text{Bi}_2\text{S}_3/\text{TiO}_2$ catalyst, the stable 2,4-D can be effectively degraded under the simulated solar light without any auxiliary oxidants such as H_2O_2 or Fenton reagents. According to the research results, a detailed degradation pathway of 2,4-D was illustrated, suggesting that hydroxyl radicals initiated by photogenerated holes are the key factor for the breaking of the 2,4-D benzene ring. By acting as photogenerated electrons acceptor and oxidant, Cr(VI) accelerates the degradation of 2,4-D.

Acknowledgments

This work is financially supported by the National Natural Science Foundation of China (Grants 51008149, 51238002, 51272099), National Natural Science Foundation of Jiangxi Province (20114BAB203018, 20122BAB203003) are acknowledged.

Appendix A. Supplementary data

Supplementary data associated with this article can be found, in the online version, at <http://dx.doi.org/10.1016/j.apcatb.2014.02.044>.

References

- [1] J.M. Herrmann, *Catal. Today* 53 (1999) 115–129.
- [2] M.N. Chong, B. Jin, C.W.K. Chow, C. Saint, *Water Res.* 44 (2010) 2997–3027.
- [3] J. Zhao, X.D. Yang, *Build. Environ.* 38 (2003) 645–654.
- [4] Z.G. Zou, J.H. Ye, K. Sayama, H. Arakawa, *Nature* 414 (2001) 625–627.
- [5] M.R. Hoffmann, S.T. Martin, W. Choi, D.W. Bahnemann, *Chem. Rev.* 95 (1995) 69–96.
- [6] (a) A. Fujishima, K. Honda, *Nature* 238 (1972) 37–38;
(b) T. Inoue, A. Fujishima, S. Konishi, K. Honda, *Nature* 277 (1979) 637–638.
- [7] I.K. Konstantinou, T.A. Albanis, *Appl. Catal. B: Environ.* 49 (2004) 1–14.
- [8] U.I. Gaya, A.H. Abdullah, *J. Photochem. Photobiol. C: Photochem. Rev.* 9 (2008) 1–12.
- [9] M. Pelaez, N.T. Nolan, S.C. Pillai, M.K. Seery, P. Falaras, A.G. Kontos, *Appl. Catal. B: Environ.* 125 (2012) 331–349.
- [10] R.J. Nelson, C.L. Flakker, D.S. Muggli, *Appl. Catal. B: Environ.* 69 (2007) 189–195.
- [11] I. Paramasivam, H. Jha, N. Liu, P. Schmuki, *Small* 8 (2012) 3073–3103.
- [12] C.A. Grimes, G.K. Mor, *TiO₂ nanotube Arrays: Synthesis, Properties, and Applications*, Springer, New York, 2009.
- [13] L.X. Yang, Y. Xiao, S.H. Liu, Y. Li, Q.Y. Cai, S.L. Luo, G.M. Zeng, *Appl. Catal. B: Environ.* 94 (2010) 142–149.
- [14] L.X. Yang, D.M. He, Q.Y. Cai, *J. Phys. Chem. C* 111 (2007) 8214–8217.
- [15] Y. Bessekhouad, D. Robert, J.V. Weber, *J. Photochem. Photobiol. A: Chem.* 163 (2004) 569–580.
- [16] X. Li, H.L. Liu, D.L. Luo, J.T. Li, Y. Huang, H.L. Li, Y.P. Fang, Y.H. Xu, L. Zhu, *Chem. Eng. J.* 180 (2012) 151–158.
- [17] J. Kim, M. Kang, *Int. J. Hydrogen Energ.* 37 (2012) 8249–8256.
- [18] L.X. Yang, Y.B. Ding, S.L. Luo, Y. Luo, F. Deng, Y. Li, *Semicond. Sci. Technol.* 28 (2013) 1–11.
- [19] M.R. Enan, *PhD Am.-Eurasian J. Sustain. Agric.* 3 (2009) 452–459.
- [20] S. Horikoshi, H. Hidaka, N. Serpone, *J. Photochem. Photobiol. A: Chem.* 159 (2003) 289–300.
- [21] E. Piera, J.C. Calpe, E. Brillas, X. Domènech, J. Peral, *Appl. Catal. B: Environ.* 27 (2000) 169–177.
- [22] C.Y. Kwan, W. Chu, *Water Res.* 37 (2003) 4405–4412.
- [23] R.J. Kieber, J.D. Willey, S.D. Zvalaren, *Environ. Sci. Technol.* 36 (2002) 5321–5327.
- [24] J.J. Testa, M.A. Grela, M.I. Litter, *Environ. Sci. Technol.* 38 (2004) 1589–1594.
- [25] L. Dupont, E. Guillon, *Environ. Sci. Technol.* 37 (2003) 4235–4241.
- [26] U. Förstner, G.T.W. Wittmann (Eds.), *Metal Pollution in the Aquatic Environment*, 2nd rev., Springer-Verlag, Berlin/New York, 1981.
- [27] D.P. Das, K. Parida, B.R. De, *J. Mol. Catal. A: Chem.* 245 (2006) 217–224.
- [28] J. Liang, Y. Zheng, J. Chen, J. Liu, D. Hulicova-Jurcakova, M. Jaroniec, S.Z. Qiao, *Angew. Chem. Int. Ed.* 124 (2012) 3958.
- [29] I.N. Martyanov, S. Uma, S. Rodrigues, K.J. Klabunde, *Chem. Commun.* 21 (2004) 2476–2477.
- [30] S. Sakthivel, B. Neppolian, M.V. Shankar, B. Arabindoo, M. Palanichamy, V. Murugesan, *Sol. Energy Mater. Sol. Cells* 77 (2003) 65–82.
- [31] J. Peller, O. Wiest, P.V. Kamat, *J. Phys. Chem. A* 105 (2001) 3176–3181.
- [32] A.L. Linsebigler, G.Q. Lu, J.T. Yates, *Chem. Rev.* 95 (1995) 735–758.
- [33] N. Wang, L.H. Zhu, Y.P. Huang, Y.B. She, Y.M. Yu, H.Q. Tang, *J. Catal.* 266 (2009) 199–206.
- [34] W.J. Kim, D. Pradhan, B.K. Min, Y. Sohn, *Appl. Catal. B: Environ.* 147 (2014) 711–725.